HHS Public Access

Author manuscript

Nat Med. Author manuscript; available in PMC 2014 February 27.

Published in final edited form as:

Nat Med. 2013 August ; 19(8): 1030–1038. doi:10.1038/nm.3246.

Suppressing aberrant GluN3A expression rescues NMDA receptor dysfunction, synapse loss and motor and cognitive decline in Huntington's disease models

Sonia Marco[1,#], **Albert Giralt**[2,#], **Milos M. Petrovic**[1,9], **Mahmoud A. Pouladi**[3,4], **Rebeca Martínez-Turrillas**[1], **José Martínez-Hernández**[5], **Linda S. Kaltenbach**[6], **Jesús Torres-Peraza**[2], **Rona K. Graham**[3,11], **Masahiko Watanabe**[7], **Rafael Luján**[5], **Nobuki Nakanishi**[8], **Stuart A. Lipton**[8], **Donald C. Lo**[6], **Michael R. Hayden**[3,4,10], **Jordi Alberch**[2], **John F. Wesseling**[1], and **Isabel Pérez-Otaño**[1]

[1]Cellular Neurobiology and Neurophysiology Laboratories, Centro de Investigación Médica Aplicada (CIMA) y Universidad de Navarra, 31008 Pamplona, Spain

[2]Department of Cellular Biology, Immunology and Neuroscience, Medical School, IDIBAPS, University of Barcelona, and Centro de Investigación Biomédica en Red sobre Enfermedades Neurodegenerativas (CIBERNED), Spain

[3]Centre For Molecular Medicine and Therapeutics, Child and Family Research Institute, University of British Columbia, Vancouver, Canada

[4]Translational Laboratory in Genetic Medicine (TLGM), Department of Medicine, National University of Singapore, and Agency for Science, Technology and Research (A *STAR), Singapore

[5]Departamento de Ciencias Médicas, CRIB-Facultad de Medicina, Universidad de Castilla-La Mancha, Albacete, Spain

[6]Center for Drug Discovery and Department of Neurobiology, Duke University Medical Center, Durham, USA

Correspondence to: Isabel Pérez-Otaño.

[11]Current address: Research Center on Aging, Department of Physiology and Biophysics, University of Sherbrooke, Canada

[#]These authors contributed equally to this work.

Supplementary on-Line Information: Supplementary Figures S1-S8
Supplementary Table S1

Author Contributions: S.M. performed and analyzed the biochemical experiments in cultured neurons, recombinant cells and YAC128 mice, the imaging experiments in cultured neurons, the spine morphology measurements, and collaborated with A.G. on neuropathological studies. A.G. performed and analyzed biochemical experiments in human, R6/1 and knock-in mice, and behavioral experiments. M.M.P. performed electrophysiological recordings. M.A.P. performed and analyzed behavioral experiments. R.M.T. contributed to mouse genotyping, and conducted biochemical fractionation and real-time PCR assays. J.M.H. and R.L. performed and analyzed electron microscopy studies. L.K. and D.C.L. performed and analyzed slice culture experiments. J.T.P. performed initial biochemical experiments in R6/1 mice. M.R.H. and R.K.G. provided the YAC128 mice. N.N. and S.A.L. provided the *GluN3A*$^{-/-}$ mice. M.W. made the GluN3A antibody used in biochemical and immunocytochemical analyses. J.A. designed and supervised experiments. J.F.W. designed and analyzed electrophysiological and fluorescence colocalization experiments, and contributed to the writing. I.P.O. conceived the study, designed experiments, analyzed data and wrote the paper.

Competing Interests Statement: The authors declare that they have no competing financial interests.

[7]Department of Anatomy, Hokkaido University School of Medicine, Sapporo, Japan

[8]Del E. Webb Center for Neuroscience, Aging and Stem Cell Research, Sanford-Burnham Medical Research Institute, La Jolla, California, USA

[9]Institute of Medical Physiology, School of Medicine, University of Belgrade, Serbia

[10]Teva Pharmaceutical Industries Ltd, Petah Tikva, Israel

Abstract

Huntington's disease is caused by an expanded polyglutamine repeat in huntingtin (Htt), but the pathophysiological sequence of events that trigger synaptic failure and neuronal loss are not fully understood. Alterations in NMDA-type glutamate receptors (NMDARs) have been implicated, yet it remains unclear how the Htt mutation impacts NMDAR function and direct evidence for a causative role is missing. Here we show that mutant Htt re-directs an intracellular store of juvenile NMDARs to the surface of striatal neurons by sequestering and disrupting the subcellular localization of the GluN3A subunit-specific endocytic adaptor PACSIN1. Overexpressing GluN3A in wild-type striatum mimicked the synapse loss observed in Huntington's disease mouse models, whereas genetic deletion of GluN3A prevented synapse degeneration, ameliorated motor and cognitive decline, and reduced striatal atrophy and neuronal loss in the YAC128 model. Furthermore, GluN3A deletion corrected the abnormally enhanced NMDAR currents, which have been linked to cell death in Huntington's disease and other neurodegenerative conditions. Our findings reveal an early pathogenic role of GluN3A dysregulation in Huntington's disease, and suggest that therapies targeting GluN3A or pathogenic Htt-PACSIN1 interactions might prevent or delay disease progression.

Huntington's disease (HD) is a progressive neurodegenerative disorder with severe motor, cognitive and psychiatric disturbances that is caused by expansion of a polyglutamine repeat within the N-terminal region of Htt. Mutant Htt (mHtt) accumulates as oligomeric species and aggregates throughout the neuronal soma and dendrites[1-3], triggering synaptic failure and loss later followed by death of subsets of striatal and cortical neurons. Limitations in understanding the mechanisms underlying Htt toxicity, especially at early stages, have been a major obstacle to finding a treatment.

A prevalent hypothesis is that mHtt engages in aberrant protein interactions, interfering with the function of key cellular components. But Htt interacts with a large network of proteins[4,5] and discerning the pathogenic interactions has proven difficult. Nevertheless, a prominent group of Htt-interactors comprises proteins involved in clathrin-mediated endocytosis[6,7], pointing towards altered protein trafficking as a key pathological mechanism.

One of these interactors, PACSIN1/syndapin1, works as an endocytic adaptor for neuronal NMDARs[8]. NMDARs play crucial roles in remodeling and maintaining excitatory synapses and their activity is altered in striatal medium-sized spiny neurons (MSNs) of transgenic mice expressing mHtt[9-13]. Because MSNs are the population first affected in HD and NMDAR dysfunction can be detected from early stages, this alteration has long been thought as a pathogenic trigger[14]. Intriguingly, PACSIN1 targets GluN3A subunits, which prevent premature synapse plasticity and stabilization during early stages of postnatal brain

development, but are down-regulated in adult brains[15,16]. In addition, the binding affinity of PACSIN1 for Htt depends on the length of the polyglutamine expansion[17], fulfilling a key criteria for pathogenic interactions[18], and PACSIN1 gain-of-function suppresses mHtt toxicity in *Drosophila* screens[4]. Thus, we hypothesized that mHtt might interfere with the endocytic removal of GluN3A-containing NMDARs by PACSIN1, leading to age-inappropriate synapse destabilization during HD pathogenesis.

Here we confirm that mHtt binds and sequesters PACSIN1 away from its normal cellular locations, causing accumulation of juvenile GluN3A-containing NMDARs at the surface of striatal neurons. We then show that GluN3A levels are abnormally elevated across mouse models of HD and in human HD striatum, and that GluN3A overexpression in mice drives degeneration of afferent synapses onto MSNs. Importantly, suppressing GluN3A reactivation in corrected the early enhancement of NMDAR currents in MSNs from YAC128 mice, prevented both early-stage and progressive dendritic spine pathology, and ameliorated later motor and cognitive decline. Our results reveal a new mechanism that mediates NMDAR dysfunction and synapse loss in HD—dysregulation of the expression of NMDARs that contain juvenile GluN3A subunits by altered endocytic trafficking, and identify a potential safe target for pharmacological therapy.

Results

PACSIN1 binds to mHtt and is sequestered into aggregates

We began by verifying the interaction between Htt and PACSIN1[4,17] with coimmunoprecipitation assays on striatal lysates from wild-type and YAC128 mice, which express full-length human *HTT* with 128 CAG repeats[19]. Although PACSIN1 interacted with both Htt variants, the interaction was stronger in YAC128 striatum (2.23 ± 0.3 fold increase in PACSIN1 bound to Htt relative to wild-type, $P = 0.005$, Fig. 1a). Coimmunoprecipitation assays from HEK293 cells co-transfected with PACSIN1 and GFP-tagged Htt exon-1 fragments that spanned the proline-rich domain that binds PACSIN1[17] and a normal or expanded polyglutamine tract (Htt^{ex1}17Q-GFP and Htt^{ex1}46Q-GFP) confirmed the polyglutamine dependence of the interaction, and additionally showed that exon-1 is sufficient for PACSIN1 binding (Fig. 1b,c). Specificity for Htt rather than the polyglutamine tract was demonstrated by experiments where PACSIN1 did not interact with either normal or expanded ataxin1, a polyglutamine repeat protein involved in spinocerebellar ataxia (Fig. 1c).

We next assessed whether binding to mHtt interferes with PACSIN1 localization or function in a cellular model of HD[20]. Cultured rat striatal neurons were transfected with Htt^{ex1} fragments, and PACSIN1 localization evaluated by immunofluorescence. Htt^{ex1}46Q-GFP formed detectable intracellular aggregates in ∼ 25% of neurons within 24–48 h, whereas Htt^{ex1}17Q-GFP exhibited diffuse expression (Supplementary Fig. 1). PACSIN1 immunostaining was punctate and distributed evenly in somatodendritic compartments of untransfected and Htt^{ex1}17Q-GFP-expressing neurons (Fig. 1d), but was enriched in somatodendritic Htt aggregates in neurons expressing Htt^{ex1}46Q-GFP (Fig. 1d,e, Supplementary Fig. 1). A quantitative colocalization analysis[21] yielded highly significant intensity correlation coefficient (ICQ) values for Htt^{ex1}46Q-GFP and PACSIN1 (0.26 ±

0.02, $P_{sign\ test} < 0.005$). Lower ICQ values were obtained for Htt^{ex1}17Q-GFP (0.065 ± 0.01), consistent with the weaker binding in biochemical assays. Other endocytic proteins were not enriched in aggregates (Fig. 1f), ruling out non-specific sequestration.

Redistribution into mHtt^{ex1} aggregates was associated with reductions of endogenous PACSIN1 levels within their normal postsynaptic location, as quantified by decreases in dendrite-to-soma fluorescence intensity ratios and consistent with dendritic depletion of PACSIN1 in humans with HD[17] (Supplementary Fig. 2a,b). Total PACSIN1 levels were unchanged (Supplementary Fig. 2c), indicating that reduced dendritic availability reflects altered subcellular distribution.

Increased surface GluN3A in neurons expressing mHtt

Because PACSIN1 controls the endocytic removal of GluN3A-containing NMDARs[8], the stronger binding and/or subcellular sequestration by mHtt might be expected to interfere with ongoing endocytosis and affect plasma membrane expression. To test this, we co-transfected striatal neurons with HA-tagged GluN3A and Htt^{ex1} variants and measured surface HA-GluN3A levels 48 h later using fluorescence-based antibody uptake assays. Htt^{ex1}46Q-GFP expression resulted in elevated surface GluN3A (Fig. 2a,b) and concomitant increases in surface levels of the obligatory NMDAR subunit GluN1 (Fig. 2c), likely reflecting GluN1 assembly with GluN3A subunits which is required for their plasma membrane transport and localization[22]. Notably, increases in GluN3A were observed both in neurons with diffuse and aggregated Htt^{ex1}46Q-GFP expression (Fig. 2b) suggesting that aggregation is not required and that binding to soluble mHtt species may be sufficient to alter PACSIN1 function. Supporting specificity for mHtt, polyglutamine expansions in ataxin1 did not alter surface GluN3A (Fig. 2d). Because alterations in bulk endocytic recycling have been reported after mHtt expression in PC12 cells[23], we analyzed transferrin uptake but found no alterations in neurons transfected with Htt^{ex1}46Q-GFP by 48 h, time when GluN3A levels were significantly elevated (Supplementary Fig. 2d,e). Nor did Htt^{ex1}46Q-GFP affect the surface levels of the AMPA receptor subunit GluA1 (Fig. 2e), which are highly reliant on endocytic recycling[24]. These results indicate that GluN3A accumulation is not due to a general impairment in neuronal endocytosis.

Knockdown of PACSIN1 using an anti-PACSIN1 short hairpin RNA (sh-PACSIN1, Supplementary Fig. 3) also increased surface GluN3A levels (Fig. 2f,g), demonstrating that PACSIN1 depletion can account for the mHtt-induced increase in surface GluN3A. We then asked whether exogenous supply of PACSIN1 could counteract the effect of mHtt. Indeed, co-transfection of PACSIN1 rescued the surface accumulation of GluN3A subunits, which returned to control levels in Htt^{ex1}46Q-GFP expressing neurons (Fig. 2a,h). These results show that loss of PACSIN1 function, likely due to mHtt binding, increases the surface expression of GluN3A-containing NMDARs in cultured striatal neurons.

Increased GluN3A in human HD striatum and mouse HD models

GluN3A is highly expressed in the brain during early postnatal and juvenile stages (P8-P15 in mice and first years of life in humans) but expression declines afterwards[25,26]. Quantitative immunoblot analysis showed that GluN3A undergoes a sharper down-

regulation in mouse striatum relative to other brain regions, with expression largely reduced into adulthood (Supplementary Fig. 4). In contrast, no developmental changes were observed in GluN2B, the predominant NMDAR subunit type in striatum (Supplementary Fig. 4). These results support a physiological role for GluN3A down-regulation in striatal NMDAR function and predict significant effects of disruption. To evaluate whether GluN3A dysregulation occurs in humans, we analyzed postmortem brain tissue from controls and HD individuals. GluN3A levels in control human putamen, a sub-region of the striatum, were low, but a significant increase in GluN3A was detected in affected individuals (Fig. 3a).

We next used the R6/1 and YAC128 mouse models of HD to evaluate the timing of GluN3A changes and association with pathogenic events. R6/1 mice, which express N-terminally truncated human *HTT* carrying 115 CAG repeats[27], displayed a progressive increase in striatal GluN3A levels relative to wild-type starting around 12–16 weeks of age (Supplementary Fig. 5a). Because PACSIN1 is enriched at synapses where it mediates GluN3A removal[8,28], we biochemically isolated synaptic plasma membranes (SPMs) to determine whether increased GluN3A levels reflect increased residency at synaptic compartments associated with changes in PACSIN1 localization. Indeed, a large increase in GluN3A levels (∼2.5 fold) was detected in SPMs from 20 week-old R6/1 mice, matching a reduction in the synaptic abundance of PACSIN1 (Fig. 3b,c).

Similar results were obtained in 3 month-old YAC128 mice (Supplementary Fig. 5b, Fig. 3d-e). Increased GluN3A levels in striatal SPMs were paralleled by increases in GluN1 and GluN2B, suggesting that GluN3A forms heteromultimeric NMDAR complexes including these subunits (Fig. 3d), and were associated with reduced synaptic PACSIN1 levels (Fig. 3e). No changes in GluN2A or GluA2/3, presynaptic proteins such as synaptophysin, or the trafficking regulators Rab4 or Rab11 were detected (Fig. 3d,e). Further fractionation of striatal synaptic membranes showed increased GluN3A in both detergent-soluble (non-PSD) and insoluble (PSD) fractions, consistent with the subsynaptic localization pattern characteristic of GluN3A[8] (Supplementary Fig. 6). Overall PACSIN1 protein expression was unchanged (0.93 ± 0.03 of wild-type, $P = 0.19$), corroborating our culture data and further indicating that lower synaptic levels of PACSIN1 reflect subcellular redistribution. At this early stage, GluN3A levels were not altered in brain regions affected later in HD such as cortex and hippocampus (Supplementary Fig. 5b). Immunolabeling further showed that GluN3A increases mainly occurred in DARPP-32 labeled MSNs (Supplementary Fig. 5c,d).

To test whether elevated GluN3A reflects a defect in endocytosis as predicted if subcellular sequestration of PACSIN1 by mHtt is the mechanism, striatal slices from control and YAC128 mice were incubated with the membrane-impermeable cross-linker BS3. This reagent cross-links surface receptors to form high molecular weight complexes that can be separated from unlinked intracellular receptors by electrophoresis, allowing a quantification of the internal receptor pool (Fig. 3f). These experiments revealed a significantly reduced fraction of intracellular GluN3A in YAC128 striatum but, again, no changes in GluA2/3 (Fig. 3f,g). We additionally looked for contributions of altered transcription but found no significant changes in GluN3A mRNA in either R6/1 or YAC128 striatum at times when synaptic and surface levels of GluN3A protein were increased by ∼2 fold (Supplementary

Fig. 5e). These results confirm that GluN3A is redistributed to the plasma membrane and synaptic compartments in mouse models of HD. They further show that striatal GluN3A dysregulation begins before or around the onset of motor or cognitive symptoms[29-32], long preceding neuronal loss, and may thus be an early disease mechanism in HD pathophysiology. Increases in GluN3A preceding symptom onset were also observed in a third HD model, the Hdh^{Q111} knock-in mice, where the phenotype is much delayed[33] (Supplementary Fig. 5f).

Suppressing GluN3A corrects NMDAR dysfunction in YAC128 mice

Alterations in NMDAR function have been reported in MSNs of YAC128 mice by 1 month. The defect involves long-lasting responses to glutamate release and has been attributed to increased activation of extrasynaptic NMDARs[13]. Because: i) a distinguishing feature of GluN3A-containing receptors is their peri- and extrasynaptic localization[8,34], and ii) GluN3A levels were increased early in synaptosomal subfractions from YAC128 striatum that are enriched in extrasynaptic plasma membrane receptors (non-PSD), we asked whether the electrophysiological defect could be explained by the elevated GluN3A levels. We crossed YAC128 mice with *GluN3A*$^{-/-}$ mice and compared NMDAR responses after intense paired pulse afferent stimulation in wild-type, YAC128 and YAC128 mice lacking GluN3A following the protocol by Milnerwood *et al*[13]. Isolated NMDAR responses were obtained by calculating the difference between responses recorded in the absence and then presence of the NMDAR blocker APV. No changes were detected in the AMPAR-mediated component obtained in APV, but large differences were detected in the decay kinetics of the isolated NMDAR-component ($P < 0.005$, YAC128 vs wild-type, Fig 3h,i), confirming previous observations[13]. Differences were largely abolished in YAC128 mice lacking GluN3A (Fig 3h,i), indicating that GluN3A is required for the mHtt-induced enhancement in NMDAR currents and consistent with the possibility that aberrant expression underlies the earliest events of HD pathophysiology.

Suppressing GluN3A rescues synapse pathology in YAC128 mice

Dendritic dystrophy and loss of glutamatergic spiny synapses are early degenerative changes in HD[7,35,36] that might underlie symptom onset. Because enhancement of GluN3A function in the hippocampus drives synapse elimination[16], we asked whether aberrant GluN3A expression could contribute to the synaptic pathology. We first used Golgi impregnation techniques to measure dendritic spines, sites where excitatory synapses form, in YAC128 mice at times when GluN3A levels were elevated (Fig. 4a). Spine numbers were decreased in dendrites of YAC128 MSNs by 3 months (13–15% decrease *vs* wild-type) and the decay worsened with age (Supplementary Fig. 7).

To test whether abnormal accumulation of GluN3A in adult MSNs could explain the progressive spine loss induced by mHtt, we measured spine densities in transgenic mice that overexpress GluN3A into adulthood (dt GFP-GluN3A[16,34]). MSNs from dt GFP-GluN3A displayed a pattern of spine loss remarkably similar to YAC128 mice (∼11% decrease *vs* single-transgenic littermates by 3 months with larger spine losses at later stages, Fig. 4b,c).

We then reasoned that if the spine loss in MSNs was caused by enhanced GluN3A function, it should be prevented by lowering GluN3A levels. To test this, we re-examined spine densities in wild-type and YAC128 mice in the presence and absence of GluN3A. Lack of GluN3A prevented both the early reductions in spine numbers in YAC128 mice, and the progressive synaptic disconnection detected as a larger loss of MSN spines at later disease stages (Fig. 4d,e). In contrast, spine densities were not altered in MSNs from adult *GluN3A*$^{-/-}$ mice (Fig. 4d,e), indicating that blocking GluN3A expression targets the synaptic pathology in HD without affecting basal spine levels in controls. This result differs from the increased spine density reported in *GluN3A*$^{-/-}$ cortical neurons[15] and likely reflects the lower GluN3A levels retained in adult striatum (Supplementary Fig. 4).

At higher resolution, electron microscopy revealed a marked loss of asymmetric glutamatergic synapses onto MSNs of YAC128 mice, which was likewise rescued by GluN3A deletion (Fig. 4f,g). In addition, postsynaptic densities were smaller in YAC128 mice (Fig. 4g), consistent with earlier studies where GluN3A overexpression decreased synapse size[16], and the deficit was also rescued by suppressing GluN3A (Fig. 4g). These results show that diminished synaptic connectivity in MSNs from YAC128 mice begins at early stages, matching the timing of GluN3A dysregulation, and can be rescued by deleting GluN3A or replicated by transgenically overexpressing GluN3A.

Suppressing GluN3A ameliorates motor and cognitive dysfunction

We next assessed the impact of GluN3A on HD-like symptoms using striatum-dependent motor and cognitive tasks. YAC128 mice showed impaired motor learning by 10 months, as indicated by increased failures when learning a fixed-speed rotarod task, and impaired coordination as represented by a shorter latency to fall from an accelerating rotarod. Both deficits were improved in YAC128 mice lacking GluN3A (Fig. 5a,b). A vertical pole test, another measure of motor coordination, showed that YAC128 mice spent less time in the pole than wild-type, an effect that was again rescued by GluN3A deletion (Fig. 5c). Nevertheless, the hypokinetic phenotype exhibited by YAC128 mice in an open-field was still apparent in YAC128 mice lacking GluN3A (Fig. 5d). Neither weight gain nor loss of muscle tone was rescued by GluN3A deletion (Supplementary Fig. 8), ruling out that improvements in coordination resulted from reversal of these parameters.

Cognitive function was evaluated using a swimming T-maze task[37]. YAC128 mice exhibited a pronounced impairment during the learning phase, whereas YAC128 mice lacking GluN3A performed as well as wild-type (Fig. 5e,g). On day 4, the platform was switched to the opposite arm of the T-maze to probe reversal (strategy-shifting) learning. YAC128 required longer than wild-type to reach the new platform location in all trials, and the defect was rescued by GluN3A deletion (Fig. 5f,g).

Suppressing GluN3A rescues mHtt toxicity

To investigate whether abnormally increased GluN3A contributes to later striatal atrophy and MSN degeneration, we performed stereological analyses in 16 month-old mice, age when neuronal death can be reproducibly detected in the YAC128 model[19]. Suppressing GluN3A expression in YAC128 mice rescued striatal atrophy and reductions in NeuN- and

DARPP-32-positive neurons (Fig. 6a,b,d). It also normalized DARPP-32 levels in surviving MSNs (Fig. 6c,d); DARPP-32 is a key component of MSN dopamine signaling cascades which is down-regulated in HD mouse models from early stages[38].

Analogous analyses in control and dt GFP-GluN3A transgenic mice showed that GluN3A overexpression *per se* does not cause striatal atrophy or neuronal loss by 16 months of age (Fig. 6e,f), but mimics neuropathological features of HD including reductions in the size of MSNs[39] (Fig. 6g) and in striatal DARPP-32 levels[40] (single-transgenic, 100 ± 16; dt GFP-GluN3A, 61 ± 5, $P < 0.05$, Fig. 6h). Finally, we conducted experiments in a rat corticostriatal slice model[41] to test whether increased GluN3A levels influence the susceptibility of MSNs to mHtt toxicity. Slice explants were co-transfected with expanded Htt^{ex1} (Htt^{ex1}73Q-GFP) along with GluN3A, and MSN degeneration was assessed by co-expression of yellow fluorescent protein. The number of surviving MSNs was decreased in brain slices co-transfected with mHtt and GluN3A relative to slices transfected with mHtt alone (Fig. 6i). Thus, increased GluN3A recapitulates features of HD neuronal dysfunction such as MSN shrinkage and disturbed signaling, and renders MSNs more vulnerable to mHtt toxicity.

Discussion

We identify a novel early-stage disease mechanism that underlies NMDAR dysfunction and synapse loss in HD: subcellular sequestration of the endocytic adaptor PACSIN1 by mHtt leaves an overabundance of juvenile NMDARs containing GluN3A subunits in the plasma membrane and postsynaptic sites of striatal neurons. The new mechanism provides a missing link between two major phenomena previously known to be impaired by Htt mutations: defects in protein trafficking and impaired NMDAR transmission. GluN3A dysregulation targeted MSNs, the vulnerable population in HD striatum, and was an early feature across HD mouse models. Knocking-out GluN3A in HD mice corrected a full sequence of early-to-late pathophysiological events, demonstrating a critical role for GluN3A in disease pathogenesis *in vivo*: normalized NMDAR currents; fully prevented synapse degeneration; rescued motor and cognitive decline; and reduced striatal cell death.

The work extends previous findings pointing towards juvenile GluN3A subunits as a synapse destabilizing or pruning factor[16], and demonstrates the pathogenic effects of aberrant reactivation in the adult brain of a pruning mechanism normally restricted to developmental stages. In the normal brain, PACSIN1-mediated retrieval of GluN3A from synapses contributes to receptor down-regulation and is thought to provide a critical signal for synaptic plasticity and growth and for robust information storage, by allowing the replacement of juvenile with mature NMDAR subtypes[8,16]. Factors that inhibit PACSIN1 function, such as dominant-negative variants of PACSIN1[8] or mHtt, increase surface and synaptic GluN3A yielding a higher proportion of small, immature synapses. Although the precise mechanisms by which mHtt alters PACSIN1 distribution remain unclear, our observations of reduced synaptic PACSIN1 in young YAC128 mice, months before aggregates appear[42], and of surface accumulation of GluN3A in striatal neurons with no detectable Htt aggregates argue against a requirement for aggregation. This fits with current concepts linking soluble mHtt species, rather than aggregates, to cytotoxicity[20,43,44]. But

PACSIN1 redistribution into microaggregates not visible by light microscopy cannot be ruled out, and the question of whether PACSIN1 binds to particular conformations of mHtt remains open.

Regarding stoichiometry of GluN3A-containing NMDARs in HD striatum, our biochemical fractionation results indicate the presence of GluN1 and GluN2B subunits. This is consistent with: biochemical evidence for assembly of GluN3A and GluN2B subunits in striatal tissue[34]; reports attributing the enhanced NMDAR responses in YAC128 mice to GluN2B-containing NMDARs[13,45]; and our finding that suppressing GluN3A corrects the alteration. GluN3A-containing subtypes are less anchored to postsynaptic densities than conventional NMDARs (GluN1/GluN2 heteromers) and GluN3A overexpression has been shown to impair the postsynaptic stabilization of GluN2B-containing NMDARs[34], which might facilitate their diffusion towards extrasynaptic sites, providing a testable cell biological mechanism for the increased extrasynaptic GluN2B-mediated currents in YAC models[13]. Along with synapse loss and enhanced extrasynaptic NMDARs, elevated GluN3A could explain features of altered glutamatergic transmission that have been observed in presymptomatic HD mice and cannot be accounted for by the increased GluN2B-mediated currents without considering the presence of additional subunits in the receptor complex. These include anomalously reduced long-term potentiation[46-48] and decreased magnesium sensitivity of NMDAR currents[11,49]; both have been reported in GluN3A overexpressing mice[16].

An imbalance between synaptic and extrasynaptic NMDAR activity is thought to be critical for neurodegeneration because the two receptor populations signal to cell survival or death pathways respectively[50], and increased extrasynaptic activity has been linked to cell death in HD[13,43]. Enhanced GluN3A expression could contribute to cell death by driving or aggravating this imbalance in two ways. First, it might trigger activation of death pathways by increasing extrasynaptic NMDAR localization. Second, MSNs receive dense glutamatergic input from cortical axons, and the synaptic disconnection driven by GluN3A could inhibit pro-survival signaling pathways coupled to synaptic NMDAR activation[50,51]. But GluN3A-containing subtypes flux less Ca^{2+} than other NMDAR subtypes[22] and data from our own lab support a neuroprotective action of GluN3A overexpression in acute excitotoxic cell death assays[34,52], which might explain the paradoxical resistance to acute excitotoxic insults observed in HD models[53,54]. Nonetheless, aberrant GluN3A expression over the much longer time course relevant to HD (i.e., decades versus minutes) could have deleterious effects due to inhibition of synaptotrophic NMDAR activity and/or chronically disturbed signaling by extrasynaptic NMDARs activated by ambient glutamate.

In summary, our work uncovers a previously unappreciated role for GluN3A dysregulation in HD and provides a rationale for the use of therapies targeting GluN3A or PACSIN1 early in the course of the disease to ameliorate cognitive or motor problems and/or halt disease progression. An advantage of targeting GluN3A (versus other NMDAR subunits) is that it is mostly lacking in adult brains, and would allow to selectively block a pathological trait without hampering normal synaptic function.

Methods

Methods and any associated references are available in the online version of the paper

Online Methods

DNA constructs

Expression plasmids encoding Htt^{ex1} or ataxin variants fused to green fluorescent protein (GFP) were described previously[20,55]. HA-GluN1-1a was from T. Yamamoto and HA-GluA1 was from M. Ehlers. HA-GluN3A was obtained by replacing the GFP tag in GFP-GluN3A[22]. Myc-tagged and mCherry-tagged rat PACSIN1 were cloned in pRK5. A 59-bp encoding a 19-bp-long small hairpin RNA (shRNA) specific for rat and mouse PACSIN1 (sh-PACSIN1 target sequence: CCATAGAGTTCCAGACATA) or a scrambled control (sh-SCR: GATCAGTGCCAACTTAACA) were cloned into pSuper-GFP vector (OligoEngine, Seattle, WA).

Cell culture and transfection

Primary striatal neuronal cultures were prepared from E19 rat embryos[8] and transfected at DIV8 using calcium phosphate. Experiments were performed 24–48 h later.

Immunofluorescence microscopy

For immunofluorescence analysis of colocalization of endocytic proteins with Htt aggregates, Htt^{ex1}-GFP-transfected neurons were fixed with 4% sucrose, 4% paraformaldehyde in phosphate-buffered saline (PBS), permeabilized with 0.1% saponin or TX-100, 1% bovine serum albumin and 2% normal goat serum in PBS, and incubated with primary antibodies followed by incubation with Cy3-conjugated secondary antibody (1:1000, Jackson ImmunoResearch). Mouse antibodies to PACSIN1 (1:200, 611811), alpha-adaptin (1:500, 610501) and EEA1 (1:250, E41120) from BD Transduction Labs, and to TfR (1:500, Zymed, 13-6800) were used. The specificity of the PACSIN1 antibody was tested by immunofluorescence in neurons transfected with two different PACSIN1 shRNAs. Images of Htt^{ex1}-GFP transfected neurons were captured using a Coolsnap HQ camera (Photometrics) mounted on a Zeiss Axiovert 200 or a Zeiss LSM 510 confocal microscope using a 63×/1.4NA Plan-Apochromat objective.

Colocalization was quantified using a custom-made ImageJ plugin to apply the Intensity Correlation Analysis of Li *et al*[21]. Comparisons were made from pairs of single image planes through the soma or individual dendritic fragments after background subtraction in each channel. Regions of interest (ROIs) containing aggregates were drawn in somatic regions of mHtt-transfected neurons and fluorescence pixel intensities were quantified in matched ROIs in the green (GFP-Htt^{ex1}) and red (Cy3, PACSIN1) channels. The difference from the mean for each pixel intensity (R_i-R_{mean} and G_i-G_{mean} where R and G are the red and green pixel intensities), and the product of the differences [PDM = (R_i-R_{mean}) × (G_i-G_{mean})] were calculated. PDMs are positive when both and red pixel intensities vary in synchrony (i.e. both red and pixel intensities are either above or below their respective means). An intensity correlation quotient (ICQ) was then calculated that is equal to the ratio

of the number of positive PDM values to the total number of pixels. The ICQ ranges between −0.5 to 0.5 (with random staining ICQ =0; dependent staining 0 < ICQ < 0.5; segregated staining 0 > ICQ > −0.5). Image sets were analyzed only in image regions free of pixel saturation, and pixel staining pairs with double 0-level intensity values were removed. Enrichment of PACSIN1 in aggregates was additionally quantified by comparing PACSIN1 intensity levels in aggregates versus a non-aggregate ROI (Supplementary Fig. 1).

To quantify dendritic PACSIN1 expression in Htt^{ex1}-GFP transfected neurons, all individual dendritic segments in the focus plane were outlined and their average pixel intensities normalized to somatic intensity to obtain a dendrite-to-soma ratio for each transfected and untransfected neuron in the same field. For total PACSIN1 measurements, Htt^{ex1}-GFP transfected neurons were outlined in the green channel, transferred to the red channel and average intensities measured after background subtraction were compared to untransfected neurons in the same field

Immunofluorescent analysis of surface receptor expression was as described[8]. Briefly, live transfected striatal neurons were incubated with an HA antibody (1:200, Covance, MMS-101P) for 30 min at 37 °C, fixed, blocked and surface HA-receptors detected with Cy3-conjugated secondary antibody. Neurons were then permeabilized, internal HA-receptors labeled with HA antibody and detected with Alexa647 secondary antibody (1:200, Invitrogen). Wide-field fluorescence images were acquired with a Zeiss 4× or 63× objective and a CoolSnap CCD camera and analyzed with Metamorph. For quantification, neurons were outlined in the GFP channel and outlines were transferred to the red and far red channel images to obtain average intensity measurements. Surface-to-internal ratios were calculated by dividing Cy3 intensity values by Alexa647 intensity values.

Transferrin uptake assay

Striatal neurons were incubated with Alexa568-conjugated transferrin (Tf, 50 μg ml^{-1}) in serum-free media for 10 min at 37 °C. Cells were then washed with serum-free medium at 10 °C, and incubated with holotransferrin (500 μg ml^{-1}) in conditioned media to exchange the surface bound transferrin and selectively monitor the endocytosed fraction. After washing, neurons were fixed and remaining intracellular Alexa-Tf imaged. For quantification, fluorescent intensities of Alexa-Tf within three to four 50 μm dendritic segments of Htt^{ex1}-GFP transfected neurons were measured for each neuron analyzed, averaged, and normalized to transferrin uptake values of untransfected neurons in the same field.

RNA interference

HEK293 cells transfected with myc-PACSIN1 and control or PACSIN1 shRNAs were lysed and PACSIN1 levels analyzed by immunoblotting with a myc antibody (1:1000, Roche, 1667149) and normalizing to GFP band (1:5000, Clontech, clone JL-8). sh-PACSIN1 was additionally tested in striatal neurons by transfection with calcium phosphate and quantification of total endogenous PACSIN1 levels.

Human postmortem brain tissue

Samples of putamen from humans with HD and controls were obtained from Banc de Teixits Neurològics (Servei Científico-Tècnics, Universitat de Barcelona, Spain) following ethical guidelines of the Declaration of Helsinki. Informed consent was obtained from all subjects under study. GluN3A expression was analyzed in post-nuclear supernatants by Western blot as described below. A rabbit antibody generated against a fragment of mouse GluN3A expanding Aas 1041–1152 was used; the specificity of the human GluN3A band was assessed by comparison with a mouse GluN3A band absent in GluN3A knockout mice and run in parallel in the same blot.

Transgenic mice

Three HD models were used in this study: transgenic R6/1 mice expressing exon1 of human *HTT* carrying 115 CAG repeats[27], YAC128 mice (line 55 homozygotes) containing full-length human *HTT* with 128 CAG repeats[19], and Hdh^{Q111} mice, with targeted insertion of a 109 CAG repeat that extends the glutamine segment in mouse Htt to 111 residues[56]. Hdh$^{Q7/Q111}$ heterozygous males and females were intercrossed to generate Hdh$^{Q7/Q111}$ heterozygous and Hdh$^{Q7/Q7}$ control littermates. Age and genetic background matched wild-type mice were used as controls for the biochemical analysis in Fig. 3 and Supplementary Fig. 5&6, and for the initial spine analysis in Supplementary Fig. 7 (CBAxC57Bl6 littermates for R6/1, FVB/N mice for YAC128, Hdh$^{Q7/Q7}$ littermates for Hdh$^{Q7/Q111}$ mice). Transgenic mice expressing juvenile GluN3A levels through adulthood[16] (dt GFP-GluN3A) and single transgenic littermates were used in spine density and neuropathological analyses. For rescue experiments, YAC128 mice (in a FVB/N background) were crossed to *GluN3A*$^{-/-}$ mice (in a C57Bl6 background, also known as *Grin3a*$^{-/-}$[15]), yielding heterozygote mice that were then crossed to obtain wild-type, *GluN3A*$^{-/-}$, YAC128 and YAC128 × *GluN3A*$^{-/-}$ mice. Littermate offspring from both sexes were used unless otherwise indicated. Electrophysiological, spine and neuropathological experiments were replicated in several mice cohorts to minimize potential confounding effects of genetic background and, in all cases, experimenters were blind to the genotype of the mice until analysis was completed. All procedures conformed to the European Community guidelines for the care and use of laboratory animals and were approved by the Ethical Committee of the University of Navarra (in accord with the Spanish Royal Decree 1201/2005).

Biochemistry

For immunoprecipitation experiments, striatal tissue or transfected HEK293 cells were lysed in T-PER buffer (Pierce) supplemented with protease inhibitors (Roche Applied Science). Protein concentrations were measured using a BCA kit (Pierce). After preclearing, lysates were incubated with a GFP antibody (1:500, Synaptic Systems, 132002), monoclonal antibody to Htt (1:500, Chemicon, MAB2166) or ImmunoPure Rabbit or Mouse Gamma Globulin (Thermo Scientific) for 4 h at 4 °C. Antibody-bound proteins were separated by centrifugation after 2 h incubation with protein A/G Agarose beads (Pierce), washed extensively with T-PER, eluted with sample buffer (Biorad), resolved using Criterion XT 3–8% Tris-acetate precast gels (Biorad) and analyzed by immunoblotting using antibodies to

PACSIN (gift from M. Plomann, 1:10000), GFP (1:5000, Clontech, clone JL-8) or Htt (1:1000, Sigma, H7540).

Total or synaptic plasma membranes (SPMs) from mouse striatal tissue were obtained by biochemical fractionation as described[8]. Further detergent extraction of striatal synaptic plasma membranes to yield an insoluble "postsynaptic density (PSD)-enriched" fraction and a soluble "non-PSD enriched" fraction (which includes peri- and extrasynaptic receptors) was conducted using the protocol by Milnerwood *et al*[13]. Protein samples were resolved by SDS-PAGE, transferred onto PVDF membranes, and detected by immunoblot (ECL Plus, Amersham) using antibodies to: GluN1 (1:2000, MAB363), synaptophysin (1:20000, MAB5256), GluN2A (1:500, 07-632) and GluA2/3 (1:1000, AB1506) purchased from Millipore; GluN2B (1:200, NeuroMab, clone N59120), GluN3A (1:1000), PACSIN1, Rab4 (1:1000, Stressgen, ADI-KAP-GF005), Rab11 (1:1000, 610657) and DARPP32 (1:1000, 611520) both from BD Transduction Labs. Band intensities were quantified on a phosphorimager (Storm 860, Amersham) using Image-Quant 5.0 software or on a GS-800 calibrated densitometer (BioRad).

Surface cross-linking

To analyze levels of intracellular pool of glutamate receptor subunits we used the membrane impermeable cross-linker, bis(sulfosuccinimidyl)suberate (BS3, Pierce) as described previously[57]. Acute corticostriatal slices (270 μm thick) from age-matched YAC128 and FVB/N mice were allowed to recover for 45 min in Krebs buffer. Slices were then incubated 30 min at room temperature in freshly prepared BS3 (1 mg ml^{-1} in D-PBS) or D-PBS. A minimum of three slices per control or treatment groups were included for each animal. To quench remaining BS3, slices were washed three times in cold 0.1 M glycine in D-PBS and then in D-PBS. Striata were then dissected out and lysed in 0.32 M sucrose/HEPES 4 mM with protease inhibitors (Roche) and PMSF (Sigma). Intracellular pool of receptors was determined by Western blot (cross-linked surface receptor complexes are retained in the stacking gel), and normalized to total receptor (non-treated).

Brain immunohistochemistry

Mice were deeply anesthesized and perfused intracardially with 4% paraformaldehyde in 0.1 M phosphate buffer (PB, pH 7.4). Coronal brain sections (30 μm) were cut with a freezing sliding microtome and stained with antibodies to GluN3A (1:100), DARPP32 (1:1000) and NeuN (1:100, Millipore, MAB377). Antigen retrieval techniques were required to reveal endogenous GluN3A. GluN3A immunoreactivity was absent from the brain of *GluN3A*$^{-/-}$ mice, establishing the specificity of the antibody for immunohistochemistry. Binding of primary antibody was visualized with a biotin-conjugated secondary antibody followed by ABC kit (Pierce) and diaminobenzidine/H_2O_2, or with FITC and Cy3-conjugated secondary antibodies.

For stereological analysis, unbiased counting relative to genotype and condition was performed using the Computer Assisted Stereology Toolbox (CAST) software (Olympus Danmark A/S, Ballerup, Denmark) as described[58]. Briefly, striatal volume was obtained by the Cavalieri method. For counts of DARPP-32 and NeuN-positive neurons per striatum, we

used the dissector counting procedure in coronal sections 30 μm thick, and spaced 240 μm apart. For estimating mean cellular/perikaryal volumes of neurons (so-called local volumes) with design-based stereology, the "nucleator" method was used.

Real-time quantitative PCR

Total RNA from mouse striatum was isolated using TRIzol Reagent (Life Technologies). First strand cDNA was synthesized from 1 μg of total RNA starting material, using Superscript III First-Strand Synthesis System for RT-PCR (Invitrogen). Quantitative real-time PCR (qPCR) was performed using a pre-designed TaqMan® Gene Expression Assay kit (Applied Biosystems), consisting of a pair of unlabeled forward and reverse amplification primers and a TaqMan® probe with a FAM™ dye label. Briefly, qRT-PCR was assayed in a total volume of 25 μl reaction mixture containing 5 μl of diluted cDNA, 12.5 μl of 2× Taqman Universal Master Mix, 1.25 μl of the 20× Taqman Gene Expression Assay and RNAse-free water. Taqman® probes for GluN3A (Mm 01341719_m1) and glyceraldehyde-3-phosphate dehydrogenase (GAPDH) (Mm 99999915_g1) were from Applied Biosystems. Probe Mm 01341719_m1 recognizes exons 2–3 of the mouse *Grin3a* gene. PCR thermal conditions included an initial 10 min at 95 °C, followed by 40 cycles of denaturation for 15 s at 95 °C and annealing/primer elongation for 1 min at 60 °C. All qPCR reactions were run in triplicate, in two independent experiments by using the Applied Biosystems 7300 RT-PCR system. Mean cycle threshold (Ct) values for each reaction were recorded for posterior data analyses. The relative RNA expression levels were calculated using GAPDH as a control: ΔCt=Ct (GAPDH) − Ct (GluN3A). The gene expression fold change, normalized to the GAPDH and relative to the control sample, was calculated as $2\hat{\Delta}$Ct.

Electrophysiology

Methods described for Figure 1 of ref [13] were followed almost exactly except the tip diameter of the stimulating electrode was larger (~20 μm); stimulus duration was 200 μS. The distance from stimulating to recording electrode was approximately 175 μm. Temperature was 23–25° C. The intracellular solution contained (in mM) 140 Cs-gluconate, 9 NaCl, 1 $MgCl_2$, 0.2 $CaCl_2$, 1 EGTA, 10 HEPES, 2 MgATP, 0.2 LiGTP, and 5 Q×314, and the extracellular solution contained 120 NaCl, 2.5 KCl, 2 $CaCl_2$, 10 glucose, 1.25 NaH_2PO_4, 26 $NaHCO_3$, nominally 5 μM $MgCl_2$, and 20 μM glycine, 2 μM strychnine, 50 μM picrotoxin and 50 μM D-(–)-APV as indicated. Mice were 28–35 day old males, and experimenters were blind to genotype. Same results were obtained in two independent mice cohorts.

Golgi impregnation and spine quantification

Fresh brain hemispheres were processed following the Golgi-Cox method[59]. The slides were randomly coded and the experimenter was blind to genotype during image acquisition and analysis. Bright-field images of Golgi-impregnated striatal MSNs were captured with a Nikon DXM 1200F digital camera attached to a Nikon Eclipse E600 light microscope (100× oil objective). Only fully impregnated MSNs with their soma found entirely within the thickness of the section, and with at least four orders of dendrites visible, were considered

for analysis. Image z-stacks were taken every 0.5 μm and analyzed with ImageJ. Dendritic segments (> 20 μm long, average: 47.35 μm; mean range: 20–95 μm) were traced through different layers of the stack and spines counted. Spine density was calculated in 4–8 dendrites of each order per neuron and values averaged to obtain neuronal averages.

Electron microscopy

For electron microscopy mice were anesthetized and perfused with saline followed by 4% paraformaldehyde and 1.5% glutaraldehyde in PB. Then, coronal sections were cut at a thickness of 60 μm using a Leica vibration microtome through the striatum. After several washes in PB, sections were postfixed with osmium tetraoxide (1% in PB) and block-stained with uranyl acetate (1% in distilled water). Sections were then dehydrated followed by propylene oxide and flat-embedded on glass slides in Durcupan (Fluka). Striata were cut at 70 nm on an ultramicrotome (Reichert Ultracut E; Leica, Austria) and collected on 200-mesh copper grids. Staining was performed on drops of 1% aqueous uranyl acetate followed by Reynolds's lead citrate. Ultrastructural analyses were performed in a Jeol-1010 electron microscope; the genotype was unknown to the experimenter. For analysis of synapse number and size the dissector principle was applied and 15 fields of 64.392 μm^2 at the striatum of each animal were randomly acquired.

Behavioral characterization

Two independent mice cohorts (wild-type, *GluN3A*$^{-/-}$, YAC128 and YAC128 × *GluN3A*$^{-/-}$) were used. Cohort 1 was used for motor and open field assessment and included 10 month-old male mice. Cohort 2, used for testing cognitive function, included 12 month-old mice of both sexes. Body weight, muscular strength and open field activity were measured[29]. For rotarod learning assessment, mice were trained at a fixed speed of 10 rpm and subsequently tested with two trials/day spaced 1–2 h apart during three consecutive days. During this learning phase, mice falling from the rod were returned and the number of falls recorded until the addition of the latencies to fall reached a total time of 60 s per trial[13,29]. For the accelerating task, the rotarod was accelerated from 5 to 40 rpm over 5 min. The latency to fall was recorded for each of two trials and averaged. For the vertical pole test, a metal pole (1.5 cm in diameter × 50 cm long) wrapped with cloth tape was used. The mouse was placed in the center of the pole which was held in a horizontal position. The pole was then gradually lifted to a vertical position and the latency to fall measured. For the swimming T-maze test, a T-maze (dimensions: arms, 38 × 14 cm; platform, 10 × 14 cm) was filled with water to a depth of 7 cm and a submerged escape platform was located in the right arm of the maze. Mice were placed into the water at the base of the stem arm of the maze and learned the location of the escape platform. During the normal testing phase, mice received 4 trials/day spaced 45 min apart for 3 consecutive days. For reversal learning, the platform was switched to the left arm of the maze. Mice received 4 trials spaced 45 min apart. Times to reach the hidden platform were recorded.

Htt exon-1 brain slice assay

Brain slice assays for Htt^{ex1}Q73-induced neurodegeneration were as described[41]. Briefly, 250 μm thick corticostriatal brain slices from P10 Sprague-Dawley rat pups were prepared

on a vibratome and placed in interface configuration over culture medium containing 15% heat-inactivated horse serum, 10 mM KCl, 10 mM HEPES, 100 U ml^{-1} penicillin/streptomycin, 1 mM MEM sodium pyruvate, and 1 mM L-glutamine in Neurobasal A (Invitrogen) under 5% CO_2 at 32 °C. Rat pups were sacrificed in accordance with U.S. National Institutes of Health guidelines and under Duke University Medical Center Institutional Animal Care and Use Committee approval. Slices were biolistically transfected (Helios gene gun, Bio-Rad) with DNA plasmids encoding YFP, $Htt^{ex1}Q73$, and/or GluN3A, all in gWiz (Genlantis). Four days after transfection, MSNs were identified by their location within the striatum and by their characteristic dendritic arborization, and scored as healthy if they exhibited continuous YFP fluorescence throughout a cell body of normal diameter, and ≥ 2 clear and unbroken primary dendrites that were ≥ 2 cell body diameters long.

Supplementary Material

Refer to Web version on PubMed Central for supplementary material.

Acknowledgments

We thank S. Finkbeiner for the Htt constructs, H. Zoghbi for the ataxin constructs, A. Zandueta, C. Rodríguez-Viña, F. Ballesteros, X. Remírez, and M. Montañana for excellent technical help, M. Galarraga for advice with image analysis, and M. Ehlers, M. Arrasate, T. Aragón, J.A. Esteban and B.D. Philpot for critical readings of the manuscript. Work was funded by the Unión Temporal de Empresas (UTE) project at the Centro de Investigación Médica Aplicada, Gobierno de Navarra, and Spanish Ministry of Science grants (SAF2010-20636 and CSD2008-00005 to I.P.O., BFU2009-12160 to J.F.W. and SAF2011-29507 to J.A.), grants from Hereditary Disease Foundation (to I.P.O. and D.C.L.), US National Institute of Health grants P01 HD29587, P01 ES016738, and R01 EY05477 (to S.A.L.), grants from Cure Huntington's Disease Initiative and Canadian Institutes of Health Research (to M.R.H.). M.R.H., a Killam University Professor, holds a Canada Research Chair in Human Genetics.

References

1. DiFiglia M, et al. Aggregation of huntingtin in neuronal intranuclear inclusions and dystrophic neurites in brain. Science. 1997; 277:1990–1993. [PubMed: 9302293]
2. DiFiglia M, et al. Huntingtin is a cytoplasmic protein associated with vesicles in human and rat brain neurons. Neuron. 1995; 14:1075–1081. [PubMed: 7748555]
3. Schaffar G, et al. Cellular toxicity of polyglutamine expansion proteins: mechanism of transcription factor deactivation. Mol Cell. 2004; 15:95–105. [PubMed: 15225551]
4. Kaltenbach LS, et al. Huntingtin interacting proteins are genetic modifiers of neurodegeneration. PLoS Genet. 2007; 3:e82. [PubMed: 17500595]
5. Goehler H, et al. A protein interaction network links GIT1, an enhancer of huntingtin aggregation, to Huntington's disease. Mol Cell. 2004; 15:853–865. [PubMed: 15383276]
6. Qin ZH, et al. Huntingtin bodies sequester vesicle-associated proteins by a polyproline-dependent interaction. J Neurosci. 2004; 24:269–281. [PubMed: 14715959]
7. Li JY, Plomann M, Brundin P. Huntington's disease: a synaptopathy? Trends Mol Med. 2003; 9:414–420. [PubMed: 14557053]
8. Perez-Otaño I, et al. Endocytosis and synaptic removal of NR3A-containing NMDA receptors by PACSIN1/syndapin1. Nat Neurosci. 2006; 9:611–621. [PubMed: 16617342]
9. Levine MS, et al. Enhanced sensitivity to N-methyl-D-aspartate receptor activation in transgenic and knockin mouse models of Huntington's disease. J Neurosci Res. 1999; 58:515–532. [PubMed: 10533044]
10. Zeron MM, et al. Increased sensitivity to N-methyl-D-aspartate receptor-mediated excitotoxicity in a mouse model of Huntington's disease. Neuron. 2002; 33:849–860. [PubMed: 11906693]

11. Cepeda C, et al. NMDA receptor function in mouse models of Huntington disease. J Neurosci Res. 2001; 66:525–539. [PubMed: 11746372]
12. Laforet GA, et al. Changes in cortical and striatal neurons predict behavioral and electrophysiological abnormalities in a transgenic murine model of Huntington's disease. J Neurosci. 2001; 21:9112–9123. [PubMed: 11717344]
13. Milnerwood AJ, et al. Early increase in extrasynaptic NMDA receptor signaling and expression contributes to phenotype onset in Huntington's disease mice. Neuron. 2010; 65:178–190. [PubMed: 20152125]
14. Beal MF, et al. Replication of the neurochemical characteristics of Huntington's disease by quinolinic acid. Nature. 1986; 321:168–171. [PubMed: 2422561]
15. Das S, et al. Increased NMDA current and spine density in mice lacking the NMDA receptor subunit NR3A. Nature. 1998; 393:377–381. [PubMed: 9620802]
16. Roberts AC, et al. Downregulation of NR3A-containing NMDARs is required for synapse maturation and memory consolidation. Neuron. 2009; 63:342–356. [PubMed: 19679074]
17. Modregger J, DiProspero NA, Charles V, Tagle DA, Plomann M. PACSIN 1 interacts with huntingtin and is absent from synaptic varicosities in presymptomatic Huntington's disease brains. Hum Mol Genet. 2002; 11:2547–2558. [PubMed: 12354780]
18. Lim J, et al. Opposing effects of polyglutamine expansion on native protein complexes contribute to SCA1. Nature. 2008; 452:713–718. [PubMed: 18337722]
19. Slow EJ, et al. Selective striatal neuronal loss in a YAC128 mouse model of Huntington disease. Hum Mol Genet. 2003; 12:1555–1567. [PubMed: 12812983]
20. Arrasate M, Mitra S, Schweitzer ES, Segal MR, Finkbeiner S. Inclusion body formation reduces levels of mutant huntingtin and the risk of neuronal death. Nature. 2004; 431:805–810. [PubMed: 15483602]
21. Li Q, et al. A syntaxin 1, Galpha(o), and N-type calcium channel complex at a presynaptic nerve terminal: analysis by quantitative immunocolocalization. J Neurosci. 2004; 24:4070–4081. [PubMed: 15102922]
22. Perez-Otaño I, et al. Assembly with the NR1 subunit is required for surface expression of NR3A-containing NMDA receptors. J Neurosci. 2001; 21:1228–1237. [PubMed: 11160393]
23. Li X, et al. Mutant huntingtin impairs vesicle formation from recycling endosomes by interfering with Rab11 activity. Mol Cell Biol. 2009; 29:6106–6116. [PubMed: 19752198]
24. Park M, Penick EC, Edwards JG, Kauer JA, Ehlers MD. Recycling endosomes supply AMPA receptors for LTP. Science. 2004; 305:1972–1975. [PubMed: 15448273]
25. Wong HK, et al. Temporal and regional expression of NMDA receptor subunit NR3A in the mammalian brain. J Comp Neurol. 2002; 450:303–317. [PubMed: 12209845]
26. Henson MA, Roberts AC, Perez-Otaño I, Philpot BD. Influence of the NR3A subunit on NMDA receptor functions. Prog Neurobiol. 2010; 91:23–37. [PubMed: 20097255]
27. Mangiarini L, et al. Exon 1 of the HD gene with an expanded CAG repeat is sufficient to cause a progressive neurological phenotype in transgenic mice. Cell. 1996; 87:493–506. [PubMed: 8898202]
28. Qualmann B, Roos J, DiGregorio PJ, Kelly RB. Syndapin I, a synaptic dynamin-binding protein that associates with the neural Wiskott-Aldrich syndrome protein. Mol Biol Cell. 1999; 10:501–513. [PubMed: 9950691]
29. Canals JM, et al. Brain-derived neurotrophic factor regulates the onset and severity of motor dysfunction associated with enkephalinergic neuronal degeneration in Huntington's disease. J Neurosci. 2004; 24:7727–7739. [PubMed: 15342740]
30. Mazarakis NK, et al. Deficits in experience-dependent cortical plasticity and sensory-discrimination learning in presymptomatic Huntington's disease mice. J Neurosci. 2005; 25:3059–3066. [PubMed: 15788762]
31. Van Raamsdonk JM, et al. Phenotypic abnormalities in the YAC128 mouse model of Huntington disease are penetrant on multiple genetic backgrounds and modulated by strain. Neurobiol Dis. 2007; 26:189–200. [PubMed: 17276692]
32. Graham RK, et al. Levels of mutant huntingtin influence the phenotypic severity of Huntington disease in YAC128 mouse models. Neurobiol Dis. 2006; 21:444–455. [PubMed: 16230019]

33. Wheeler VC, et al. Early phenotypes that presage late-onset neurodegenerative disease allow testing of modifiers in Hdh CAG knock-in mice. Hum Mol Genet. 2002; 11:633–640. [PubMed: 11912178]
34. Martinez-Turrillas R, et al. The NMDA receptor subunit GluN3A protects against 3-nitroproprionic-induced striatal lesions via inhibition of calpain activation. Neurobiol Dis. 2012; 48:290–298. [PubMed: 22801082]
35. Graveland GA, Williams RS, DiFiglia M. Evidence for degenerative and regenerative changes in neostriatal spiny neurons in Huntington's disease. Science. 1985; 227:770–773. [PubMed: 3155875]
36. Cummings DM, Cepeda C, Levine MS. Alterations in striatal synaptic transmission are consistent across genetic mouse models of Huntington's disease. ASN Neuro. 2:e00036. [PubMed: 20585470]
37. Van Raamsdonk JM, et al. Cognitive dysfunction precedes neuropathology and motor abnormalities in the YAC128 mouse model of Huntington's disease. J Neurosci. 2005; 25:4169–4180. [PubMed: 15843620]
38. Bibb JA, et al. Severe deficiencies in dopamine signaling in presymptomatic Huntington's disease mice. Proc Natl Acad Sci U S A. 2000; 97:6809–6814. [PubMed: 10829080]
39. Vonsattel JP. Huntington disease models and human neuropathology: similarities and differences. Acta Neuropathol. 2008; 115:55–69. [PubMed: 17978822]
40. Rudnicki DD, Pletnikova O, Vonsattel JP, Ross CA, Margolis RL. A comparison of huntington disease and huntington disease-like 2 neuropathology. J Neuropathol Exp Neurol. 2008; 67:366–374. [PubMed: 18379432]
41. Reinhart PH, et al. Identification of anti-inflammatory targets for Huntington's disease using a brain slice-based screening assay. Neurobiol Dis. 2011; 43:248–256. [PubMed: 21458569]
42. Slow EJ, et al. Absence of behavioral abnormalities and neurodegeneration in vivo despite widespread neuronal huntingtin inclusions. Proc Natl Acad Sci U S A. 2005; 102:11402–11407. [PubMed: 16076956]
43. Okamoto S, et al. Balance between synaptic versus extrasynaptic NMDA receptor activity influences inclusions and neurotoxicity of mutant huntingtin. Nat Med. 2009; 15:1407–1413. [PubMed: 19915593]
44. Bodner RA, et al. Pharmacological promotion of inclusion formation: a therapeutic approach for Huntington's and Parkinson's diseases. Proc Natl Acad Sci U S A. 2006; 103:4246–4251. [PubMed: 16537516]
45. Li L, Murphy TH, Hayden MR, Raymond LA. Enhanced striatal NR2B-containing N-methyl-D-aspartate receptor-mediated synaptic currents in a mouse model of Huntington disease. J Neurophysiol. 2004; 92:2738–2746. [PubMed: 15240759]
46. Murphy KP, et al. Abnormal synaptic plasticity and impaired spatial cognition in mice transgenic for exon 1 of the human Huntington's disease mutation. J Neurosci. 2000; 20:5115–5123. [PubMed: 10864968]
47. Usdin MT, Shelbourne PF, Myers RM, Madison DV. Impaired synaptic plasticity in mice carrying the Huntington's disease mutation. Hum Mol Genet. 1999; 8:839–846. [PubMed: 10196373]
48. Lynch G, et al. Brain-derived neurotrophic factor restores synaptic plasticity in a knock-in mouse model of Huntington's disease. J Neurosci. 2007; 27:4424–4434. [PubMed: 17442827]
49. Starling AJ, et al. Alterations in N-methyl-D-aspartate receptor sensitivity and magnesium blockade occur early in development in the R6/2 mouse model of Huntington's disease. J Neurosci Res. 2005; 82:377–386. [PubMed: 16211559]
50. Hardingham GE, Bading H. Synaptic versus extrasynaptic NMDA receptor signalling: implications for neurodegenerative disorders. Nat Rev Neurosci. 11:682–696. [PubMed: 20842175]
51. Cepeda C, Wu N, Andre VM, Cummings DM, Levine MS. The corticostriatal pathway in Huntington's disease. Prog Neurobiol. 2007; 81:253–271. [PubMed: 17169479]
52. Nakanishi N, et al. Neuroprotection by the NR3A subunit of the NMDA receptor. J Neurosci. 2009; 29:5260–5265. [PubMed: 19386922]

53. Hansson O, et al. Transgenic mice expressing a Huntington's disease mutation are resistant to quinolinic acid-induced striatal excitotoxicity. Proc Natl Acad Sci U S A. 1999; 96:8727–8732. [PubMed: 10411943]

54. Graham RK, et al. Differential susceptibility to excitotoxic stress in YAC128 mouse models of Huntington disease between initiation and progression of disease. J Neurosci. 2009; 29:2193–2204. [PubMed: 19228972]

55. Irwin S, et al. RNA association and nucleocytoplasmic shuttling by ataxin-1. J Cell Sci. 2005; 118:233–242. [PubMed: 15615787]

56. Lloret A, et al. Genetic background modifies nuclear mutant huntingtin accumulation and HD CAG repeat instability in Huntington's disease knock-in mice. Hum Mol Genet. 2006; 15:2015–2024. [PubMed: 16687439]

57. Grosshans DR, Clayton DA, Coultrap SJ, Browning MD. Analysis of glutamate receptor surface expression in acute hippocampal slices. Sci STKE. 2002; 2002:PL8. [PubMed: 12072555]

58. Giralt A, Carreton O, Lao-Peregrin C, Martin ED, Alberch J. Conditional BDNF release under pathological conditions improves Huntington's disease pathology by delaying neuronal dysfunction. Mol Neurodegener. 2011; 6:71. [PubMed: 21985529]

59. Ricobaraza A, Cuadrado-Tejedor M, Marco S, Perez-Otano I, Garcia-Osta A. Phenylbutyrate rescues dendritic spine loss associated with memory deficits in a mouse model of Alzheimer disease. Hippocampus. 2012; 22:1040. [PubMed: 21069780]

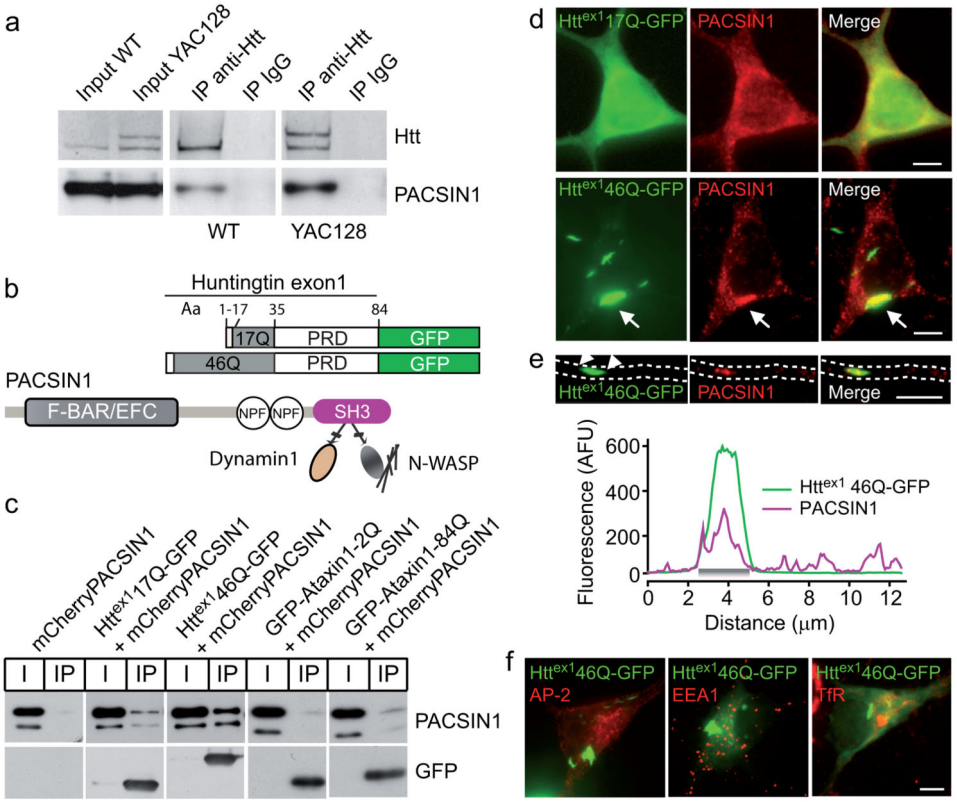

Figure 1. PACSIN1 binds to and colocalizes with mHtt

(**a**) Coimmunoprecipitation of Htt and PACSIN1 from striatal lysates of 3 month-old wild-type and YAC128 mice. Htt was immunoprecipitated with an antibody that recognizes both wild-type and mHtt. Immunoprecipitates (IP) were immunoblotted with the indicated antibodies. Additionally, 10% of the lysate (input) used for immunoprecipitation was loaded. (**b**) Scheme of PACSIN1 structure indicating the F-BAR membrane deformation domain, the NPF motifs responsible for GluN3A binding, and the C-terminal SH3 domain. The SH3 domain mediates association with the proline-rich domain (PRD) of Htt but also links PACSIN1 to proteins of the endocytic machinery such as dynamin1 and N-WASP. The location of GFP within the constructs used in this study is indicated. (**c**) HEK293 cells transfected with the indicated constructs were lysed and lysates immunoprecipitated with a GFP-specific antibody. Input lysates (I) and immunoprecipitates (IP) were immunoblotted with the indicated antibodies. (**d**) Representative images of striatal neurons transfected with Htt^{ex1}17Q-GFP or Htt^{ex1}46Q-GFP and stained for endogenous PACSIN1 48 h later. Arrow points to colocalization of mHtt^{ex1} with PACSIN1 in cytoplasmic aggregates. (**e**) Colocalization of mHtt^{ex1} and PACSIN1 in dendritic aggregates. Line scan analysis shows a large increase in PACSIN1 fluorescence at the Htt^{ex1}46Q-GFP dendritic aggregate flanked by arrowheads (grey bar in graph). (**f**) Representative images of striatal neurons transfected with Htt^{ex1}46Q-GFP and immunostained for endogenous α-adaptin (AP-2), the early endosome marker EEA1, or transferrin receptor (TfR) which labels recycling endosomes. Scale bars in all images, 5 μm.

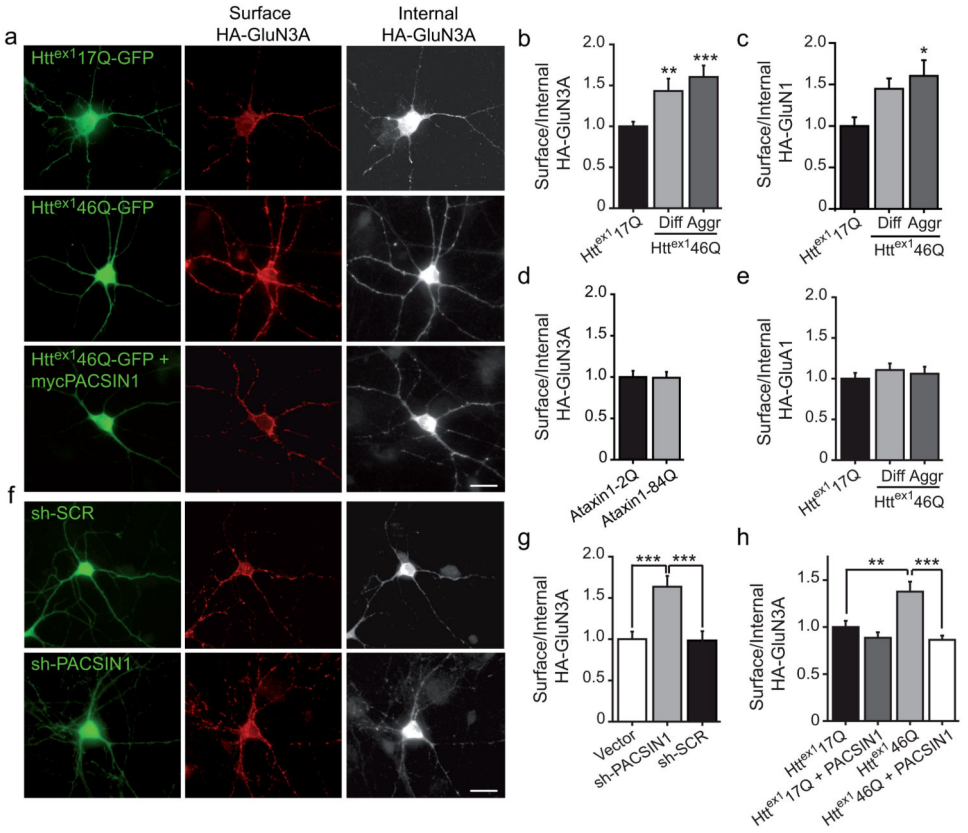

Figure 2. mHtt increases the surface expression of GluN3A-containing NMDARs

(**a**) Representative images of striatal neurons cotransfected with GFP-Htt^{ex1} and HA-tagged GluN3A with or without myc-PACSIN1. Surface (red) and internal receptors (white) were labeled with HA antibody 48 h post-transfection. Scale bar, 20 μm. (**b, c, d, e**) Quantification of GluN3A, GluN1 and GluA1 surface/internal ratios in neurons transfected with GFP-tagged Htt^{ex1} or ataxin1. In this and all subsequent figures, data are mean ± S.E.M (*n* = 20–54 neurons per condition from 2–3 independent experiments, * $P < 0.05$, ** $P < 0.01$, *** $P < 0.001$ *vs* Htt^{ex1}17Q-GFP, ANOVA followed by Bonferroni multiple comparison test). (**f**) Striatal neurons co-transfected with HA-GluN3A and anti-PACSIN1 shRNA (sh-PACSIN1) or scrambled control sh-RNA (sh-SCR). (**g**) Quantification of surface/internal HA-GluN3A ratios in neurons transfected with sh-PACSIN1. Scale bar, 20 μm (*n* = 17–52 neurons/condition from 2 independent experiments, *** $P < 0.001$, ANOVA followed by Bonferroni test). (**h**) Quantification of HA-GluN3A surface/internal ratios in Htt^{ex1}-GFP-transfected neurons after cotransfection with myc-PACSIN1 (*n* = 51–69 neurons from 4 independent experiments, ** $P < 0.01$, *** $P < 0.001$, ANOVA followed by Bonferroni test).

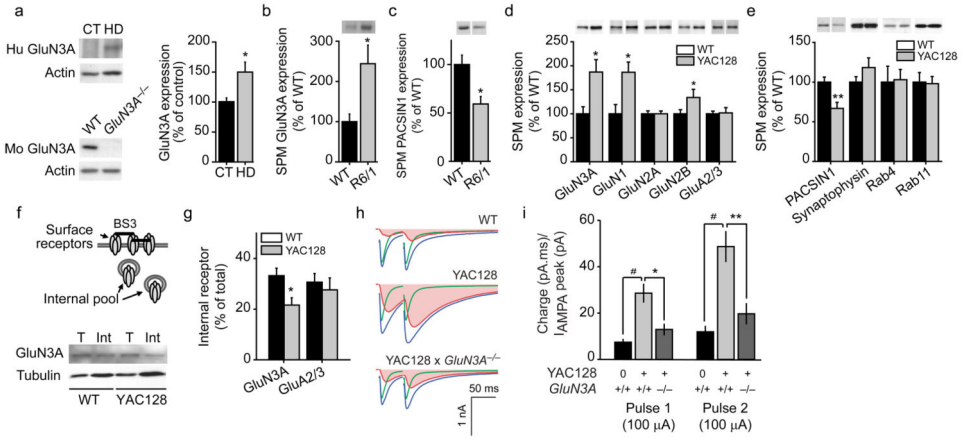

Figure 3. Enhanced GluN3A levels in the striatum of humans with HD and mouse models

(**a**) GluN3A expression in putamen samples from HD individuals and matched controls. Specificity of the GluN3A antibody was tested in *GluN3A*$^{-/-}$ mice. For quantification, optical densities of GluN3A bands were normalized to actin (n = 6 per group, * $P < 0.05$, Student's t-test). (**b**) GluN3A and (**c**) PACSIN1 levels in synaptic plasma membranes (SPMs) from striata of 16–20 week-old R6/1 mice (n = 4–5 mice per group, * $P < 0.05$, Student's t-test). (**d, e**) Expression of glutamate receptors and other synaptic proteins in SPMs from striata of 3 month-old wild-type or YAC128 mice (n = 3–11 mice per group; * $P < 0.05$; ** $P < 0.01$, Student's t-test). (**f**) Immunoblots showing GluN3A expression in striatal slices from 3 month-old YAC128 and wild-type mice, either untreated (total, T) or incubated with BS3 (internal, Int). (**g**) Quantification of internal GluN3A and GluA2/3 fraction (n = 6–8 mice per group; * $P < 0.05$, Student's t-test). (**h**) Excitatory postsynaptic currents (EPSCs) in MSNs after local afferent stimulation. Blue: compound NMDA and AMPAR responses. Green: AMPAR components (50 µM APV). Red: NMDAR components obtained by subtraction. Traces are averages across all recordings (n = 11–15 cells/slices from 6–8 mice per genotype). (**i**) Quantification of the NMDAR component of the EPSCs integrated between 5 and 49 ms after stimulation, divided by the peak of the AMPAR component (# $P < 0.005$, * $P < 0.05$, ** P <0.01, Kolmogorov-Smirnov test). No significant differences was detected between wild-type and YAC128 × *GluN3A*$^{-/-}$ and the nominal differences were caused by two outliers.

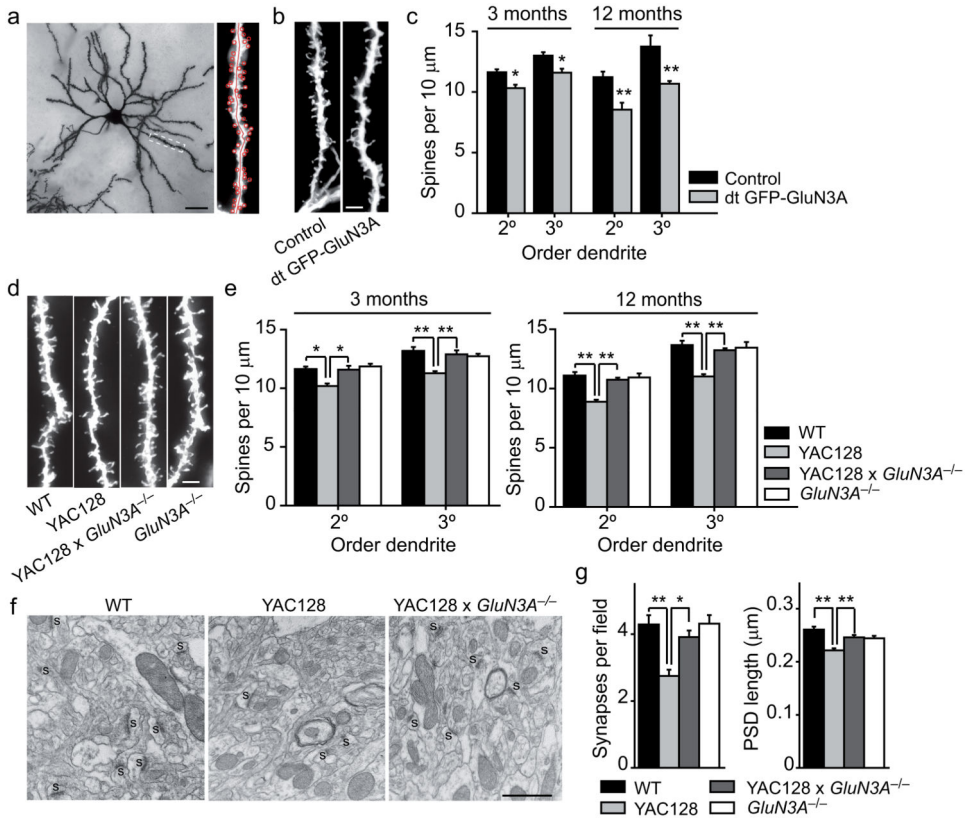

Figure 4.

Aberrant GluN3A expression in striatal MSNs triggers spine and synapse loss.

(**a**) Golgi-impregnated MSN from a wild-type mouse. The secondary dendrite in dashed area is showed at larger magnification. Spines (red circles) were counted in segments of a known length (red line) to obtain spine densities. Scale bar, 20 µm. (**b**) Representative segments of secondary dendrites from MSNs of 3 month-old control and dt GFP-GluN3A mice. Scale bar, 3 µm. (**c**) Quantification of spine densities in dt GFP-GluN3A and age-matched controls (n = 12–18 neurons from 4 mice per genotype, * $P < 0.01$, ** $P < 0.001$ vs wild-type, Student's t-test). (**d**) Dendritic segments from MSNs of 3 month-old wild-type, YAC128, YAC128 × *GluN3A*$^{-/-}$ and *GluN3A*$^{-/-}$ mice. (**e**) Quantification of spine densities in MSNs from mice of the indicated ages and genotypes (n = 24–32 neurons from 6–8 mice per group, * $P < 0.01$ ** $P < 0.001$, ANOVA followed by Bonferroni multiple comparison test). (**f, g**) Electron microscopy analysis of number and size of excitatory synapses in striatum of 3 month-old mice. Scale bar, 1 µm (n = 3 mice per genotype, * $P < 0.01$, ** $P < 0.001$ Kruskal-Wallis test followed by Bonferroni multiple comparison test; 15 fields of each animal were randomly acquired at the level of the striatum and analyzed in a blind fashion).

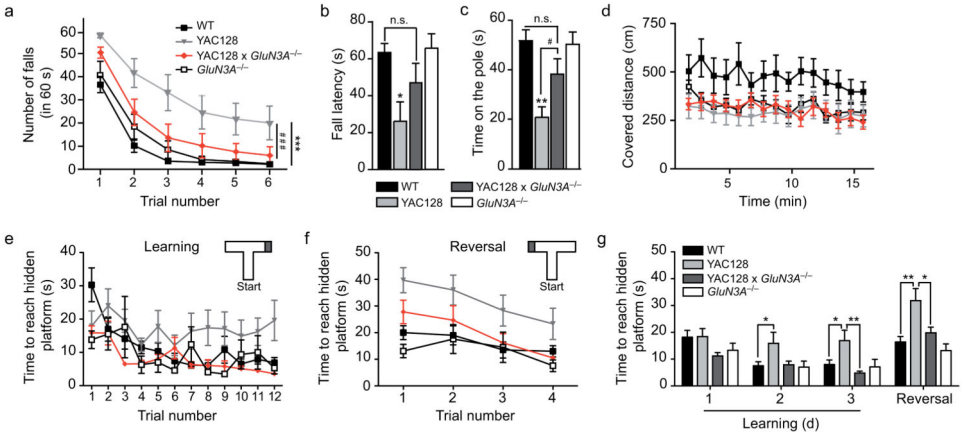

Figure 5. Rescue of motor and cognitive dysfunction by GluN3A deletion

(**a**) Number of falls from a fixed speed rotarod and (**b**) fall latency from an accelerating rotarod for 10–12 month-old mice of the indicated genotypes (n = 10 mice per genotype, * P < 0.05, *** P < 0.001 vs wild-type and *GluN3A*$^{-/-}$, ### P < 0.001 vs YAC128 × *GluN3A*$^{-/-}$, n.s. non significant; two-way ANOVA). (**c**) Time spent in the vertical pole (n = 10–13 mice per genotype, ** P < 0.01 vs wild-type and *GluN3A*$^{-/-}$; # P < 0.05 vs YAC128 × *GluN3A*$^{-/-}$; one-way ANOVA followed by Tukey's t-test). (**d**) Spontaneous locomotor activity in the open-field test. Note that knocking-out GluN3A *per se* decreases activity but the effect is not summative in the presence of mHtt (n = 10). (**e**) Times to reach the hidden platform in the swimming T-maze during the training phase (3 days, 4 trials per day) and (**f**) and after platform reversal on day 4. (**g**) Daily averages of times to reach hidden platform (n = 5–11 mice per genotype, * P < 0.05, ** P < 0.01).

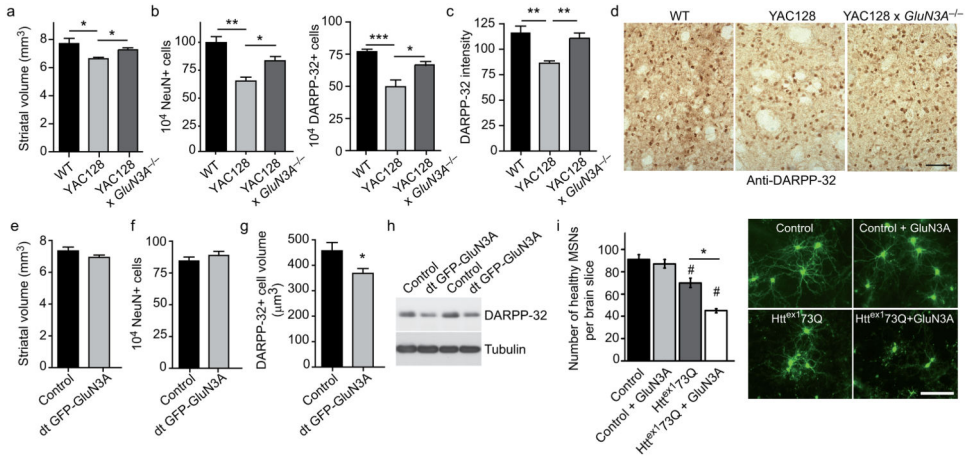

Figure 6. Suppressing GluN3A prevents, and increasing GluN3A potentiates, mHtt induced death of striatal MSNs

(**a, b**) Stereological measurements of striatal volume and number of NeuN- and DARPP-32-positive neurons in 16 month-old wild-type, YAC128, and YAC128 × *GluN3A*$^{-/-}$ mice. (**c**) DARPP-32 staining intensity levels per cell measured in surviving MSNs. (**d**) Representative microphotographs of DARPP-32 stained striata. Scale bar, 70 μm. (**e, f**) Stereological measurements of striatal volume and number of NeuN-positive neurons in 16 month-old control and dt GFP-GluN3A mice. (**g**) Measurements of cell volume in DARPP-32 positive neurons. (**h**) Immunoblots showing striatal DARPP-32 protein levels in 24 month-old control and dt GFP-GluN3A mice. Data were analyzed by one-way ANOVA followed by Tukey's test or Student's t-test when only two groups were compared (n = 6–9 mice per genotype, * $P < 0.05$, ** $P < 0.01$ and *** $P < 0.001$). (**i**) (Left panel) Ordinate axis shows number of non-degenerating MSNs per brain slice as assessed by co-expression of yellow fluorescent protein (YFP) with the indicated constructs (n = 15–18 slices scored per condition, * $P < 0.01$, # $P < 0.01$ relative to control slices, ANOVA followed by Tukey's t-test, data are representative of 3 independent experiments). (Right panel) Representative images of striatal slices in the YFP channel. Scale bar, 100 μm.